Journal of Geophysical Research: Solid Earth

Supporting Information for

Focusing effects of Teleseismic Wavefields by the Subducting Plate beneath Cascadia: Evidence for Slab Continuity

Guanning Pang[1*], Geoffrey A. Abers[1], Peter E. van Keken[2]

[1]Dept. of Earth and Atmospheric Sciences, Cornell University, Ithaca, NY 14850, USA

[2]Earth and Planets Laboratory, Carnegie Institution for Science, Washington DC 20015, USA

*Corresponding author: gp327@cornell.edu

For submission to *Journal of Geophysical Research: Solid Earth*

This supplemental document contains three text sections, 12 figures, one table, and their associate captions.

Text S1. Differential attenuation measurement

The differential attenuation operator Δt^* between paths to neighboring stations *i* and *j*, $\Delta t^*_{ij} = \Delta t^*_i - \Delta t^*_j$, can be measured from ratios and differences in signal amplitudes and phases between station pairs. Assuming no frequency dependence, the amplitude ratio (A_{ij}) and phase shift ($\Delta\phi_{ij}$) are related to the Δt^*_{ij} as (e.g., Eilon and Abers, 2017):

$$\ln\left(A_{ij}(f)\right) = k_{1ij} - \pi f \Delta t^*_{ij} \quad \text{(S1)}$$

$$\Delta\phi_{ij}(f) = k_{2ij} - \frac{1}{\pi}\ln\left(\frac{f}{f_\infty}\right)\Delta t^*_{ij} \quad \text{(S2)}$$

Where $A_{ij}(f)$ is the amplitude ratio between station *i* and *j* at frequency *f*, $\Delta\phi_{ij}(f)$ is the phase shift between station *i* and *j* at frequency *f*, k_{1ij} and k_{2ij} are constants related to the difference in station

gains and anharmonic phase velocity between station *i* and *j*, respectively, and f_∞ is a high reference frequency. Assuming $f_\infty = e^\pi$, Eq. (S2) becomes (Eilon & Abers, 2017):

$$\Delta\phi_{ij}(f) = k_{2ij} + (1 - \frac{1}{\pi}\ln(f))\Delta t^*_{ij} \quad \text{(S3)}$$

We measure the amplitude ratios, $A_{ij}(f_k)$, and phase shifts, $\Delta\phi_{ij}(f_k)$, between stations by applying a comb of narrowband filters, where f_k is the center frequency of the k^{th} filter (Dziewonski et al., 1969). The Δt_i^* at each station can be determined by minimizing the L2 norm:

$$L2 = \gamma \sum_{ijk} w_{ij}(f_k)(\ln\left(A_{ij}(f_k)\right) - \ln\left(A_{ij}^{pred}(f_k)\right))^2 + \sum_{ijk} w_{ij}(f_k)(\Delta\phi_{ij}(f_k) - \Delta\phi_{ij}^{pred}(f_k))^2 \quad \text{(S4)}$$

Where $ln\left(A_{ij}^{pred}(f_k)\right)$ and $\Delta\phi_{ij}^{pred}(f_k)$ are the predictions from Eq. (S1) and Eq. (S3), respectively. $w_{ij}(f_k)$ is the weight of the amplitude ratio and phase shift between station *i* and *j* at central frequency f_k, γ is the relative weight between the amplitude ratio and phase shift.

We applied the multi-narrow filter technique to both real data and synthetics. We use cross-correlation coefficients between signals and event medians as $w_{ij}(f)$ in the least-square inversion for real-data. The $w_{ij}(f)$ is set to 1 in all inversion scenarios for synthetics. We also set γ in Eq. (S4) to 2.0 following Soto Castaneda et al. (2021), to require higher weighting of amplitude misfit in all real data and synthetics inversion.

For real data, we apply a comb of 30 narrowband filters logarithmically spaced at center frequencies f_k from 0.05 to 2.0 Hz to a 35 s window signal starting 5 s before the *S* arrivals. Although the narrowband filters are generated up to 2 Hz, the maximum frequencies (f_{max}) used in each earthquake are varied depending on the signal-to-noise ratio and are generally lower. We calculate the frequency (f_{cross}) where the signal's amplitude spectral crosses the amplitude spectrum of the pre-event noise for each station. Then, we calculate the mean of f_{cross} of all

stations as f_{max} for each earthquake; fmax ranges from 0.296 to 0.41 Hz. Any $A_{ij}(f)$ and $\Delta\phi_{ij}(f)$ at $f > f_{max}$ are not used in the Δt* determination, and only measurements at frequencies for which cross-correlation coefficients between signals and event medians > 0.5 are used.

For synthetics, we apply a comb of 10 narrowband filters logarithmically spaced at center frequencies of 0.05–0.5 Hz. With this approach, $A_{ij}(f)$ and $\Delta\phi_{ij}(f)$ are measured for a total of 2,415 station pairs in each simulation. We use $\gamma = 2$ in the joint inversion of $A_{ij}(f)$ and $\Delta\phi_{ij}(f)$.

Text S2. Analysis of long-period amplitude

We systematically investigate the amplitude variations across the iMUSH array at ~20 s for 23 earthquakes. We stack the amplitudes at each station for four earthquakes near Japan at back azimuths of~307°, four earthquakes near Tonga-Fiji at back azimuths of ~ 230°, and eight earthquakes located in Latin America at back azimuths of ~130°, respectively. Before stacking, the amplitudes are normalized to the amplitude at station MD12 to correct the source effects. For Alaska earthquakes at back azimuths of ~298°, we first look at the amplitude variations of the Mw 6.5 earthquake that occurred on November 11, 2015 (Fig. 2d); then, we stack amplitudes for all four Alaska earthquakes. As a result, we obtain eight sets of amplitude variations across the iMUSH array. We normalize the amplitude measurements of these observations to obtain the ratios to the median amplitude of each earthquake across the iMUSH array to obtain the amplitude anomalies.

Text S3. Frequency-wave number analysis (*f-k*)

We applied the frequency-wave number analysis (*f-k*) (Rost & Thomas, 2002) to the teleseismic S wavefields recorded on transverse-component at frequencies of 0.05–0.3 Hz and calculated the power spectrum of the slowness vector (s_x, s_y) in a range of -20–20 s/° at intervals

of 0.1 s/°. The iMUSH array may have slowness anomalies from the local geological heterogeneity (Bondár et al., 1999). To account for those, we correct station arrival times with *S*-wave travel-time residuals calculated from an ambient-noise-based shear-wave velocity model of the crust and upper mantle, down to ~112 km around MSH (Crosbie et al., 2019). These static corrections are applied before we perform the slowness analysis. However, there is little effect from them and a systematic slowness anomaly remains; thus, we focus on analyzing the changes of slowness vectors with lag time after the *S* onset. We used a time window of 25 s with a sliding time step of 20 s to calculate the slowness spectrum for the first 45 s of the teleseismic *S* wavefield.

References:

Bondár, I., North, R. G., & Beall, G. (1999). Teleseismic slowness-azimuth station corrections for the International Monitoring System seismic network. *Bulletin of the Seismological Society of America*, 89(4), 989–1003.

Dziewonski, A., Bloch, S., & Landisman, M. (1969). A technique for the analysis of transient seismic signals. Bulletin of the Seismological Society of America, 59(1), 427–444.

Rost, S., & Thomas, C. (2002). Array seismology: Methods and applications. *Reviews of Geophysics*, 40(3), Art. No. 1008.

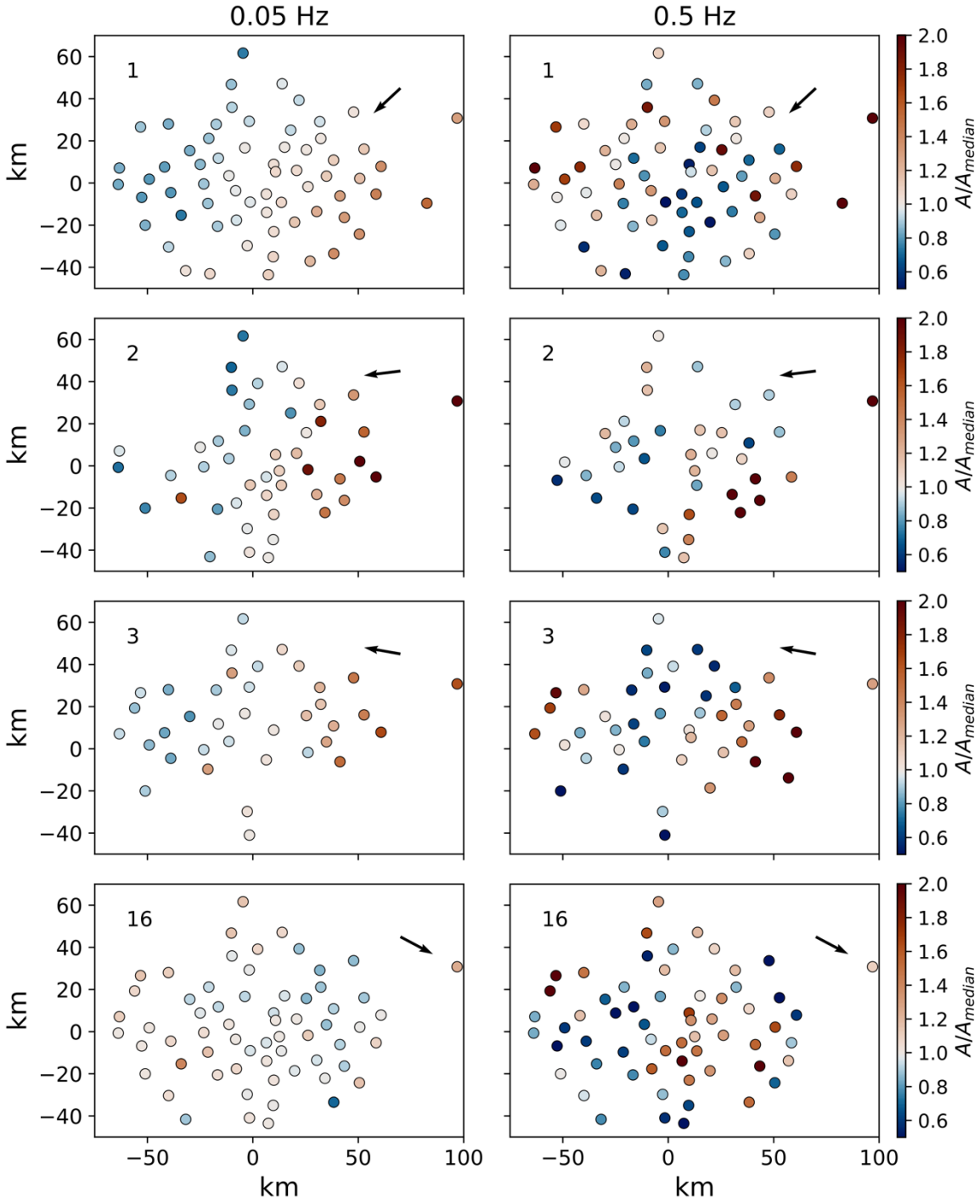

Figure S1. Amplitude variations for earthquakes 1–3 and 16 in Table S1. Left panels are the amplitude variation of *S* phases at 0.05 Hz; Amplitudes on radial-component are plotted for earthquake 1. Amplitude on transverse-component is plotted for earthquake 2 and 3. Right panels are the amplitude variations of *P* phases on Z component at 0.5 Hz. Arrows indicate the direction of wave propagation.

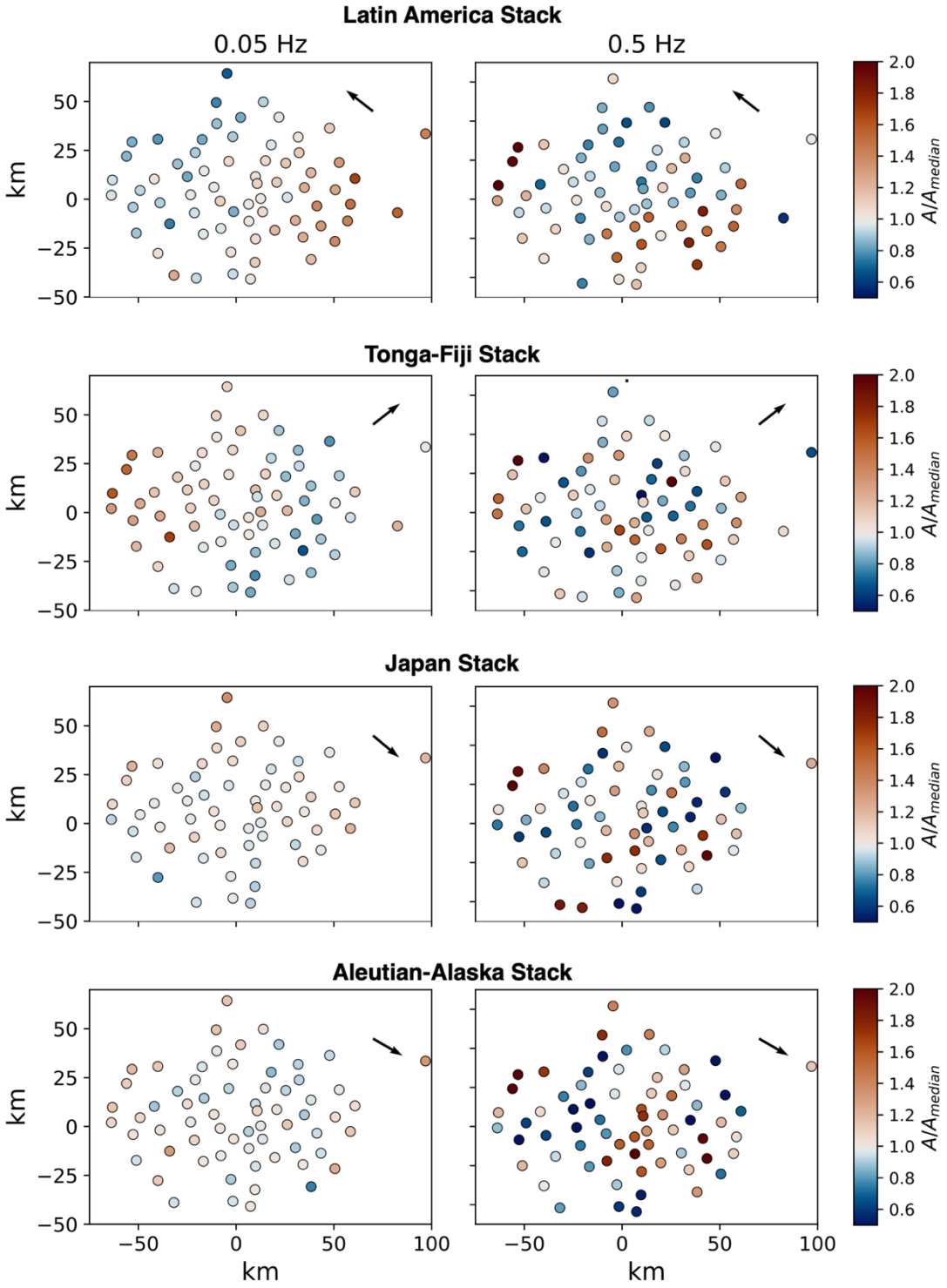

Figure S2: Similar to Fig. S1 but for stacks of earthquakes at different regions marked in subtitle. The amplitude variation of *S* phases is calculated from T component. Arrows indicate the direction of wave propagation.

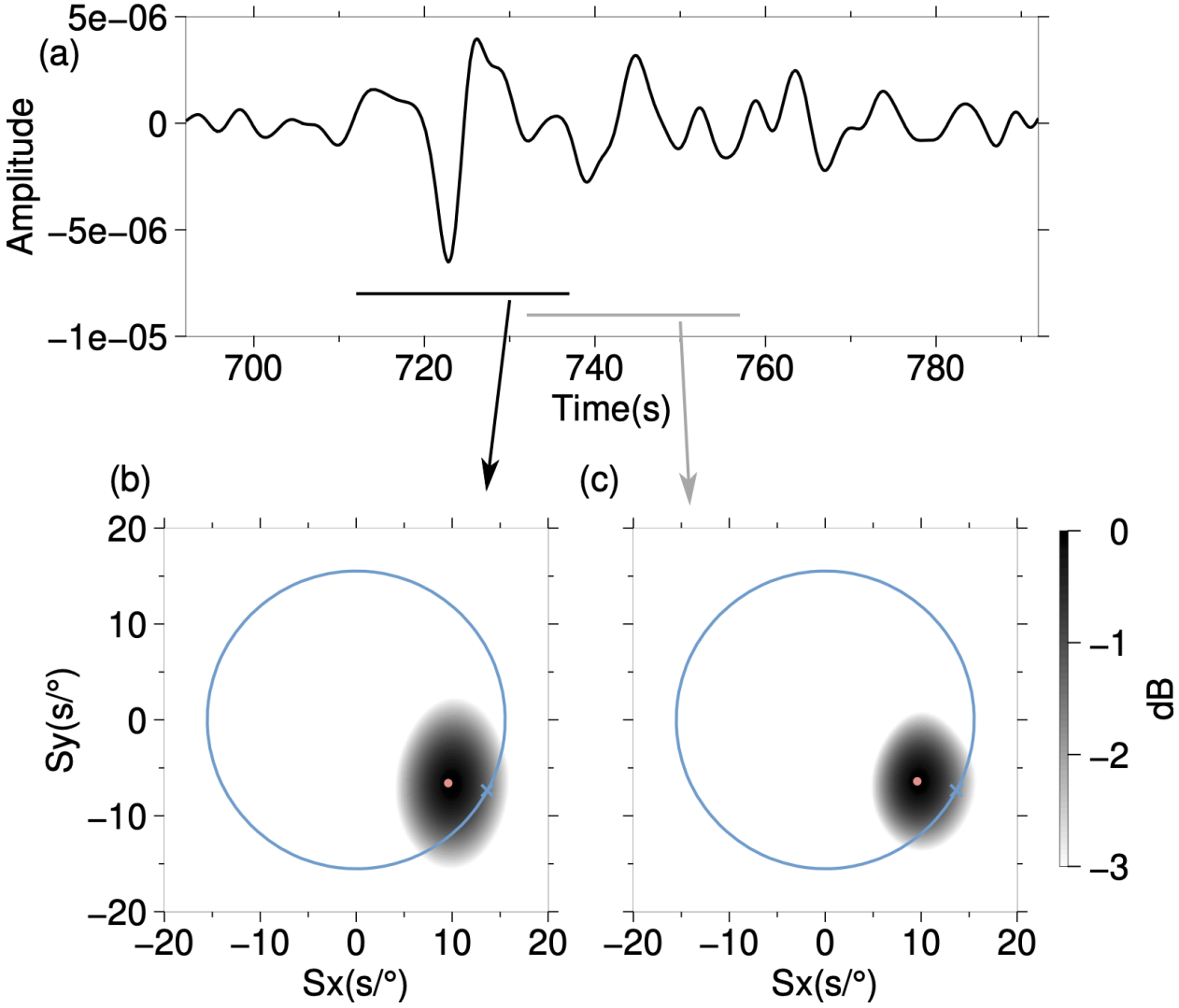

Figure S3. Similar to Fig. 4 but for an earthquake in the Alaska region shown at Fig. 2d (eq. 16 at table S1).

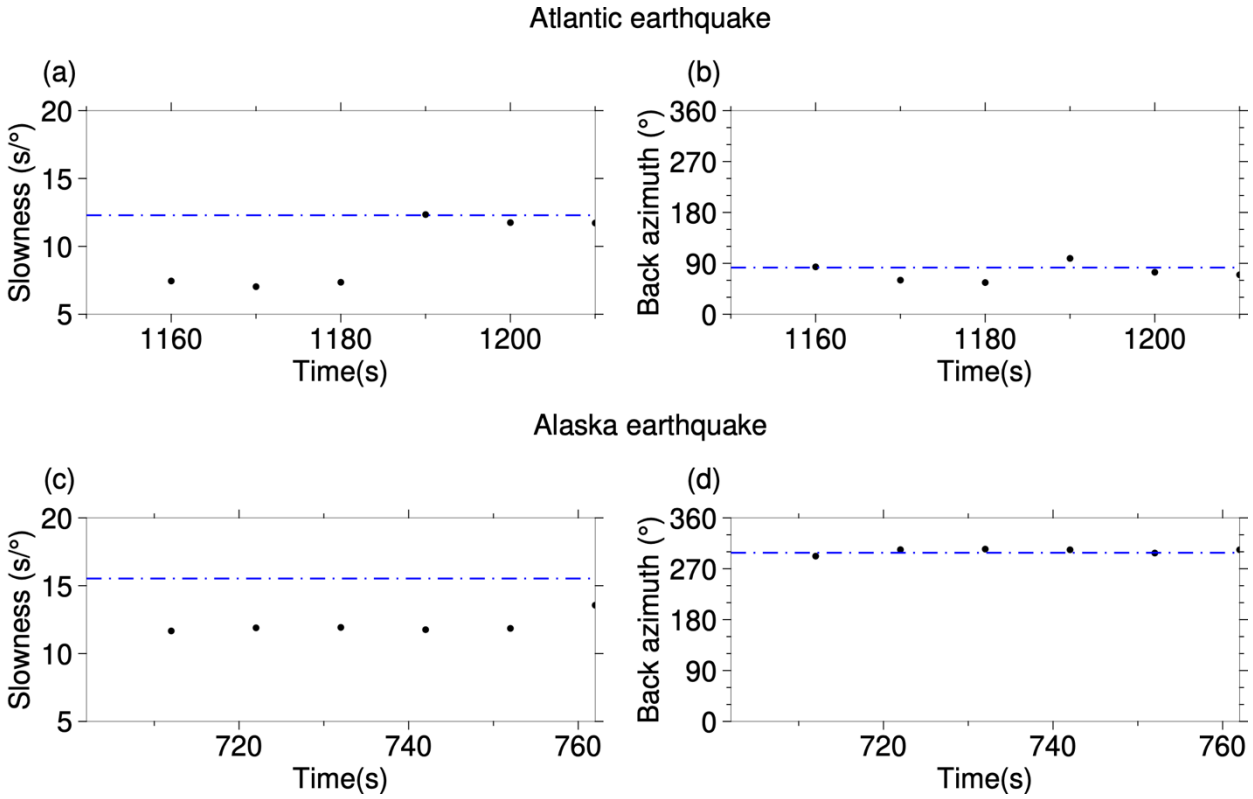

Figure S4. Sliding window results showing parameters as a function of time relative to event origin time. (a) and (b) show the slowness and back azimuth results for the Atlantic earthquake shown in Figure. 2c and 3. (c) and (d) show the slowness and back azimuth results for the Alaska earthquake shown in Figure 2d and Figure S3. Each dot is plotted in the center of the time window used in the beamforming calculation.

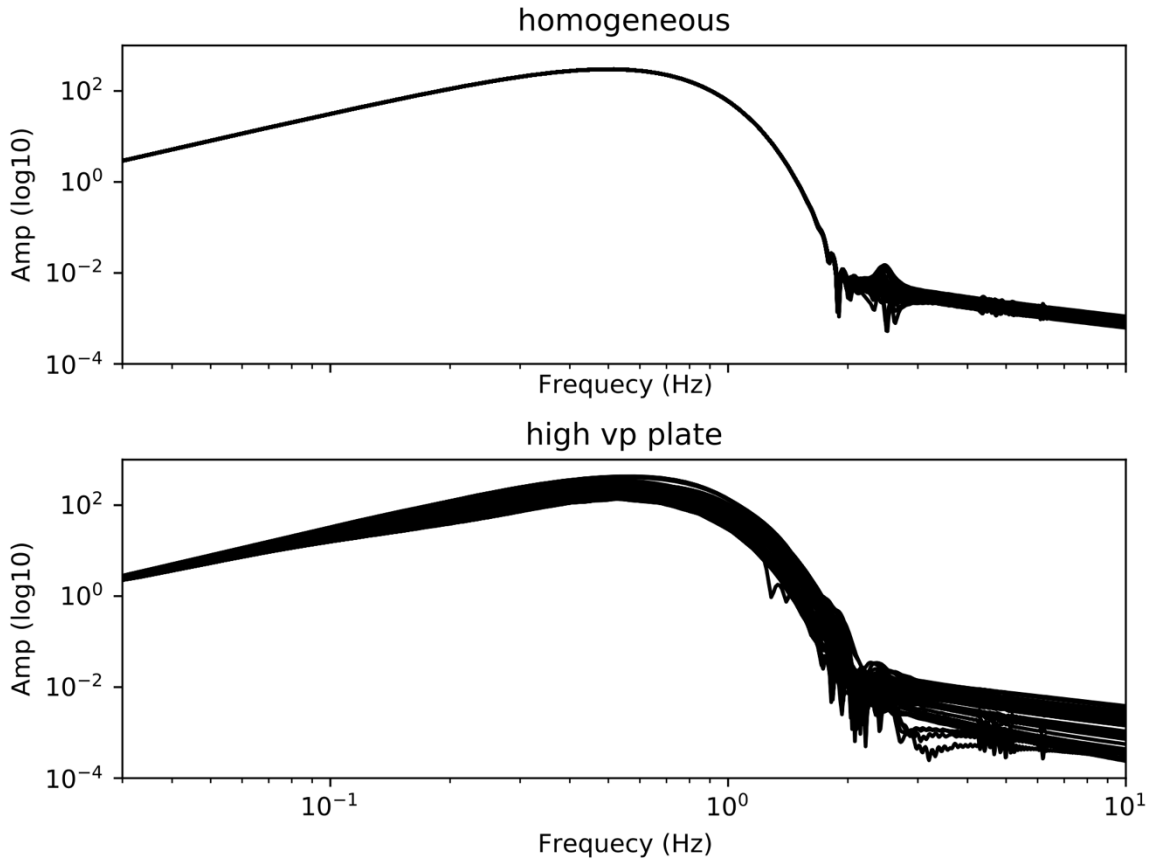

Figure S5. Amplitude spectra for synthetic waveforms at all 70 iMUSH stations from (a) homogeneous velocity model; (b) simplified slab model (Model i) (Fig. 5).

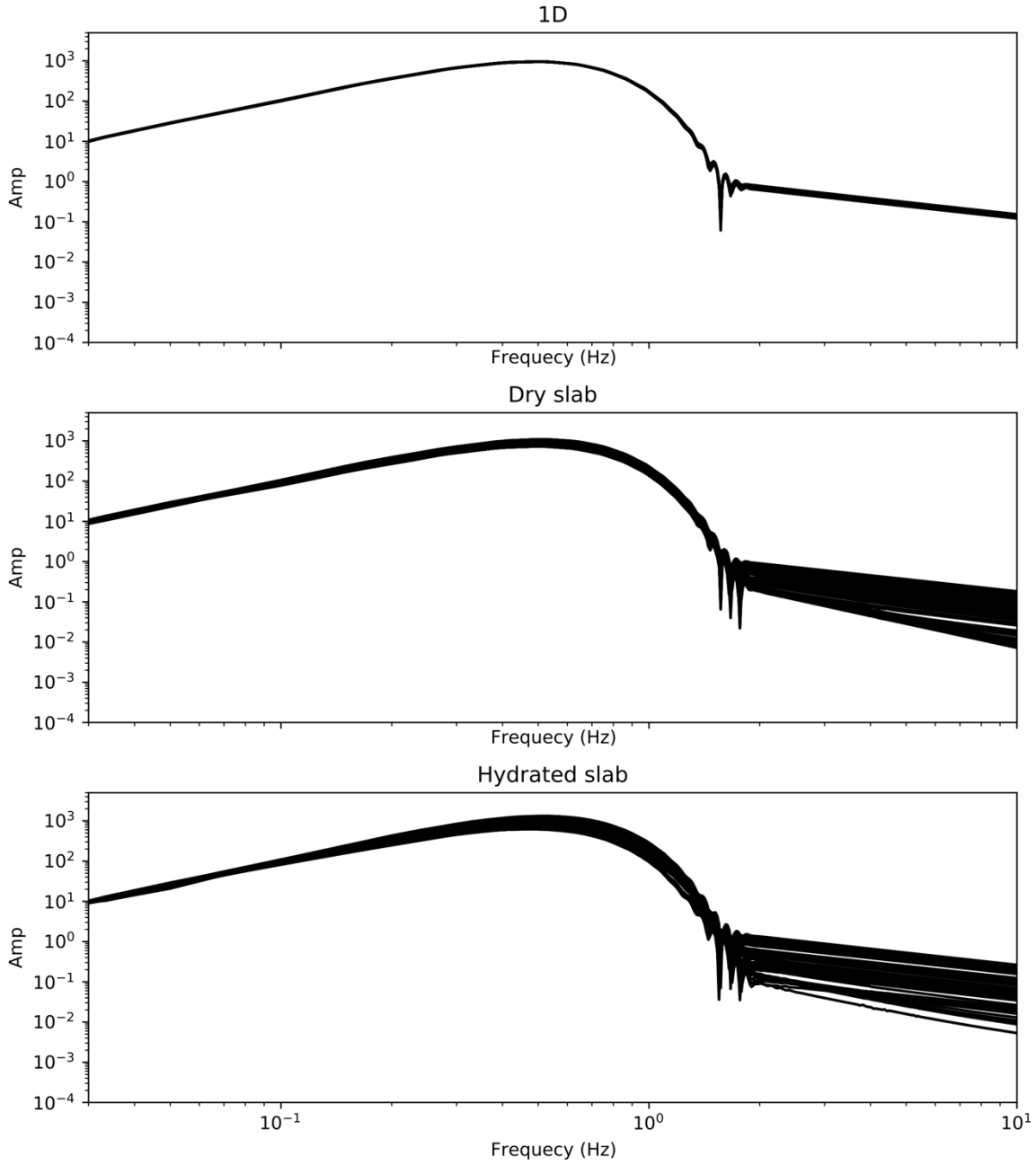

Figure S6. Amplitude spectra for synthetic waveforms at all 70 stations from (a) 1D velocity model; (b) Dry forearc mantle wedge model (Fig. 9a); and (c) Hydrated wedge model (Fig. 9c).

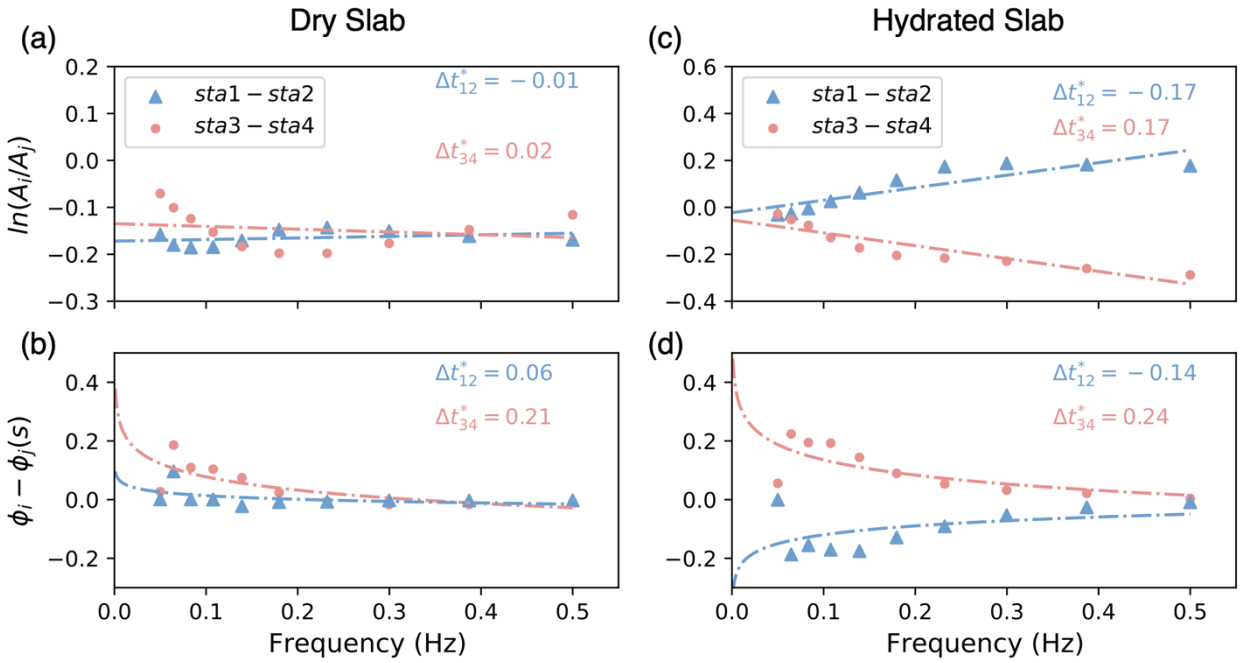

Figure S7. Examples of Δt^* measurements from synthetic waveforms between stations. (a) –(b) Differential Δt^* from amplitude ratios and phase shift, respectively, for Model ii. (c) – (d) Similar to (a) – (b) but for Model iii.

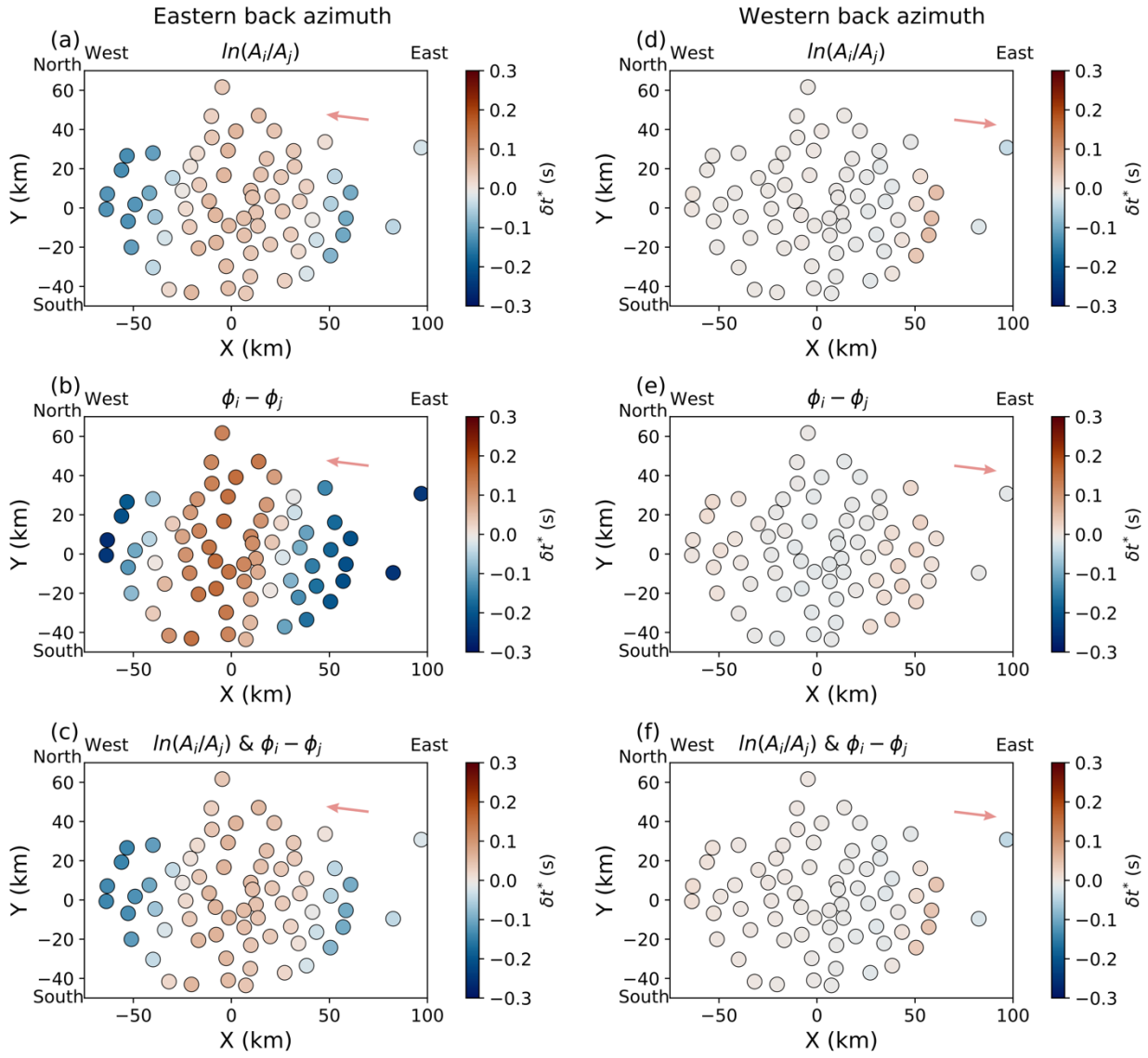

Figure S8. Similar to Figure. 8 but for Model ii.

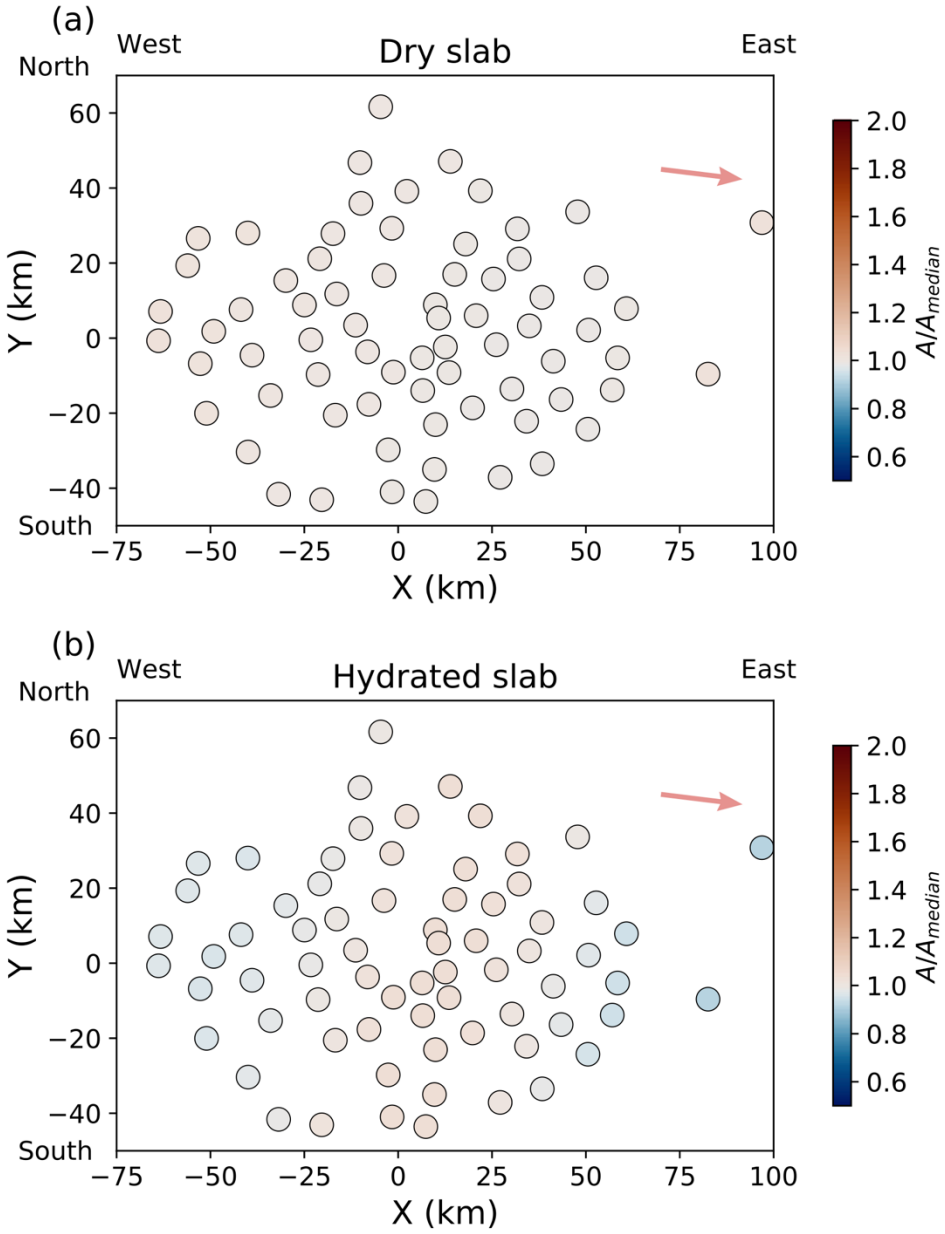

Figure S9. Similar to Figure. 9b and 9d but for the case of that the teleseismic wavefields propagate from west to iMUSH array.

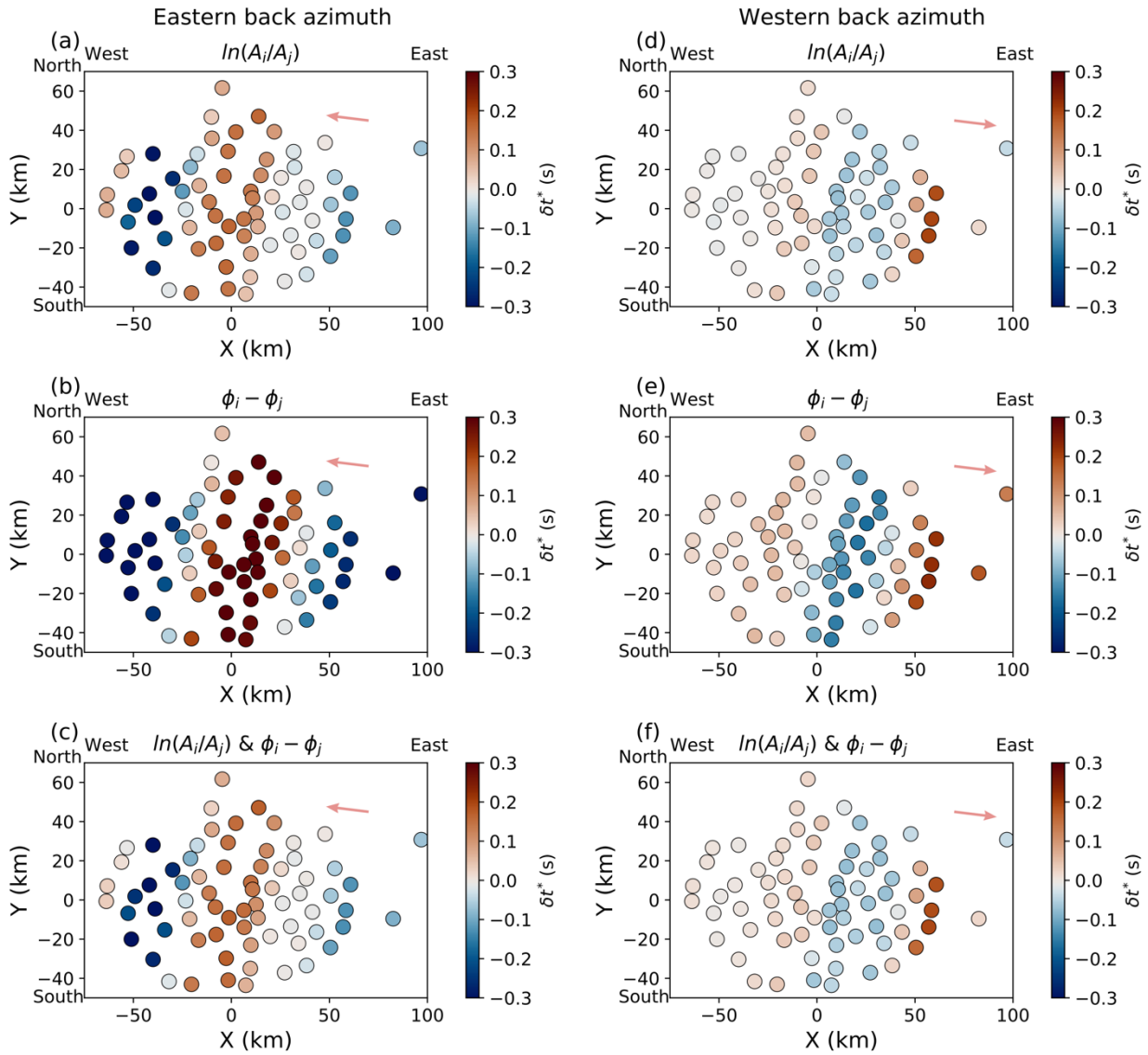

Figure S10. Similar to Figure. 8 but for Model iii.

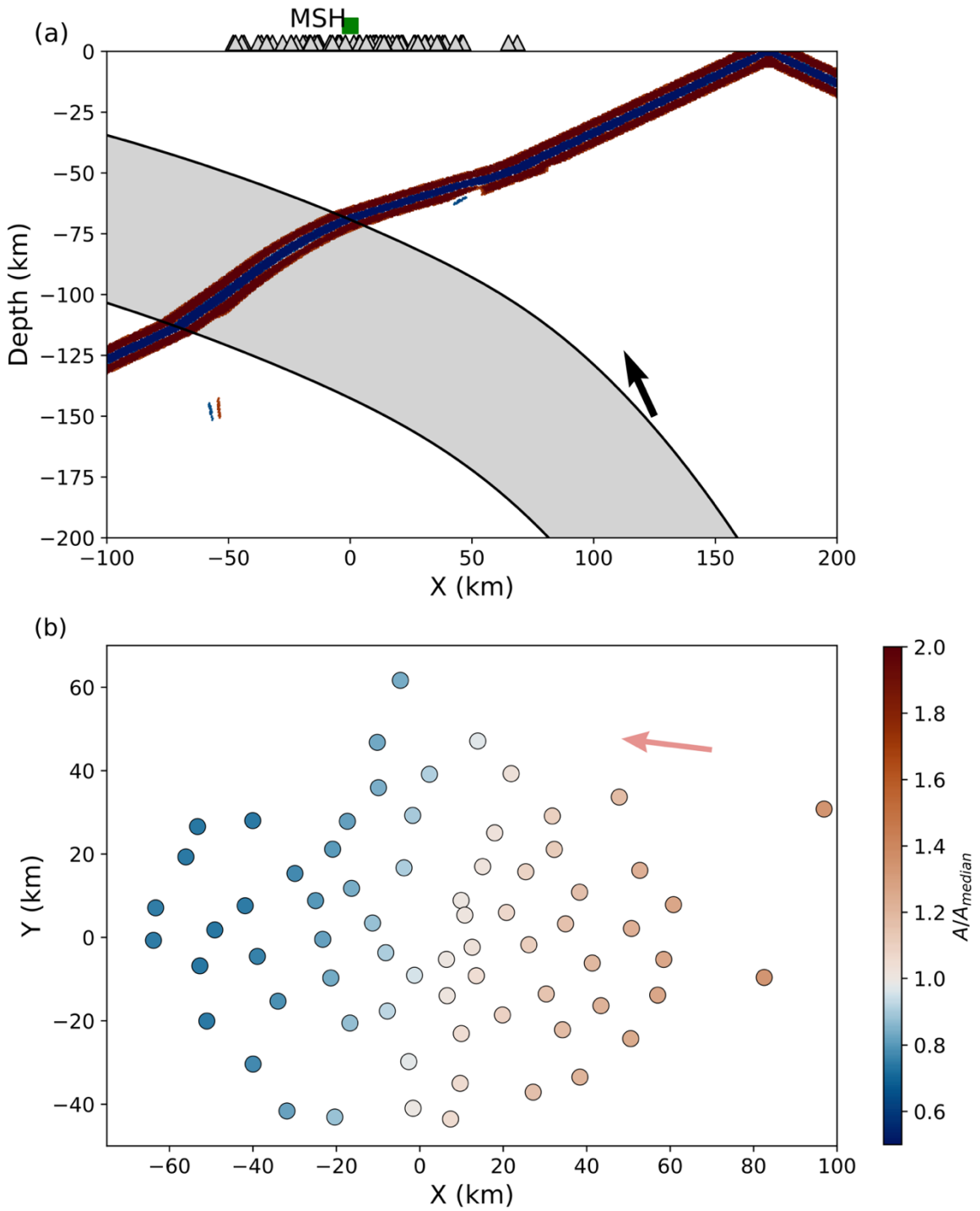

Figure S11. (a) A thicker simplified Cascadia slab model with thickness of ~ 60 km. Geometry and other symbols same as Figure. 5. (b) Similar to Figure 6c but for synthetic wavefields from model in (a)

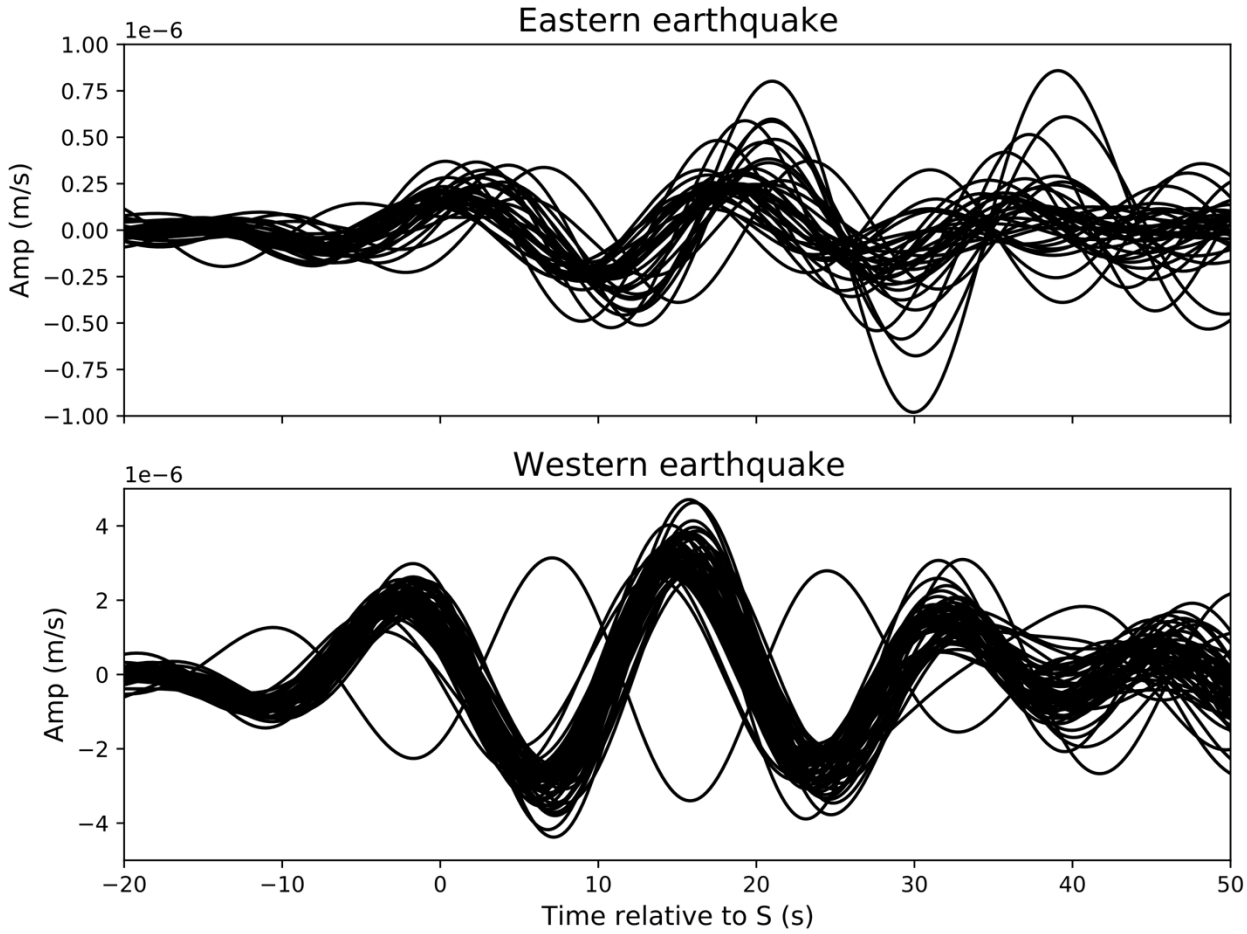

Figure S12. Transverse-component *S* waveforms filtered by a narrowband filter at 0.05 Hz. Upper panel shows waveforms for the eastern earthquake shown as dark red dot in Figure 1. Bottom panel shows waveforms for western earthquake shown as red dot in Figure 1.

Table S1. Earthquakes with amplitude variation patterns

Index	Time	Latitude (°)	Longitude (°)	Depth (km)	Magnitude	Back azimuth
1	2015-02-13T18:59:12.2	52.65	-31.9	17	7.1	48°
2	2016-06-21T16:26:34.4	22.66	-45.14	10	6.1	82°
3	2015-07-16T15:16:33.8	13.87	-58.54	20	6.4	100°
4	2014-12-08T08:54:52.5	7.94	-82.69	20	6.6	126°
5	2016-05-18T16:46:43.9	0.50	-79.62	30	6.9	128°
6	2016-05-18T07:57:02.7	0.43	-79.79	16	6.7	128°
7	2015-01-07T05:07:07.5	5.91	-82.66	8	6.5	127°
8	2016-04-16T23:58:36.9	0.35	-79.93	21	7.8	128°
9	2016-04-22T03:03:41.7	-0.29	-80.51	10	6.0	129°
10	2015-12-17T19:49:53.0	15.80	-93.63	85	6.6	132°
11	2016-04-29T01:33:38.9	10.27	-103.74	10	6.6	150°
12	2015-03-30T07:56:53.2	-15.43	-173.0	10	6.0	231°
13	2016-05-27T04:08:44.0	-20.81	-178.65	568	6.5	231°
14	2015-06-16T06:17:01.2	-20.39	-179.00	656	6.0	232°
15	2015-04-17T15:52:51.5	-15.88	-178.60	10	6.5	234°
16	2015-11-09T16:03:46.1	51.64	-173.07	15	6.5	298°
17	2016-03-19T01:35:12.2	51.51	-174.14	17	6.1	298°
18	2016-03-12T18:06:44.8	51.56	-173.94	19	6.4	298°
19	2015-07-27T04:49:46.4	52.38	-169.45	29	6.9	298°
20	2015-07-07T05:10:28.1	43.91	147.98	49	6.3	303°
21	2016-01-11T17:08:03.9	44.48	141.09	239	6.3	307°
22	2016-03-20T22:50:20.4	54.29	162.81	30	6.4	308°
23	2016-01-30T03:25:12.2	53.98	158.54	177	7.2	309°